Smith ScholarWorks

Computer Science: Faculty Publications

Computer Science

2-1-2021

Periodic Tilings and Auxetic Deployments

Ciprian S. Borcea
Rider University

Ileana Streinu
Smith College, istreinu@smith.edu

Follow this and additional works at: https://scholarworks.smith.edu/csc_facpubs

Part of the Computer Sciences Commons

Recommended Citation

Borcea, Ciprian S. and Streinu, Ileana, "Periodic Tilings and Auxetic Deployments" (2021). Computer Science: Faculty Publications, Smith College, Northampton, MA.
https://scholarworks.smith.edu/csc_facpubs/261

This Article has been accepted for inclusion in Computer Science: Faculty Publications by an authorized administrator of Smith ScholarWorks. For more information, please contact scholarworks@smith.edu

Article

MMS

Mathematics and Mechanics of Solids
1–18
© The Author(s) 2020
Article reuse guidelines:
sagepub.com/journals-permissions
DOI: 10.1177/10812865209481 16
journals.sagepub.com/home/mms
SAGE

Periodic tilings and auxetic deployments

Ciprian S Borcea
Department of Mathematics, Rider University, Lawrenceville, NJ, USA

Ileana Streinu
Department of Computer Science, Smith College, Northampton, MA, USA

Received 25 June 2020; accepted 17 July 2020 **[AQ: 1]**

Abstract
We investigate geometric characteristics of a specific planar periodic framework with three degrees of freedom. While several avatars of this structural design have been considered in materials science under the name of chiral or missing rib models, all previous studies have addressed only local properties and limited deployment scenarios. We describe the global configuration space of the framework and emphasize the geometric underpinnings of auxetic deformations. Analogous structures may be considered in arbitrary dimension.

Keywords
Periodic framework, auxetic deformation, pseudo-triangulation, chiral models, Prussian blue

1. Introduction

This paper is concerned with the geometric study of a planar periodic framework presented in its initial configuration in Figure 1. The framework is made of congruent square plates connected with rigid bars between vertices, which are considered universal joints, that is, they allow any relative rotation of plate and bar. All bars are of equal length, which is taken to be twice the edge length of a square plate. The generators of the periodicity lattice are shown as arrows and the unit cell they span is indicated with thin lines.**[AQ: 2]**

Obviously, this planar periodic plate-and-bar framework can be converted into an equivalent periodic bar-and-joint framework by retaining all vertices as joints and replacing the square plates by their four edges plus a diagonal as bars (respecting periodicity).

With hindsight, the structural pattern may be recognized in several ornamental motifs, e.g. the sixteenth-century tiles shown in Figure 2.

This *tetragonal* design, together with its *trigonal* and *hexagonal* relatives, chiral and anti-chiral subspecies, and several manufacturing variations, have been frequently studied in connection with *auxetic behavior* and *deployment scenarios* [1–7]. Auxetic behavior refers to lateral widening on stretching, or, in reverse, lateral shrinking on compression.

Our main purpose in considering this recurrently explored pattern [8–20] is to uncover the geometric features that underlie the deformation possibilities of the framework, including expansive and auxetic capabilities, area

Corresponding author:
Ciprian S Borcea, Department of Mathematics, Rider University, Lawrenceville, NJ, USA.
Email: borcea@rider.edu

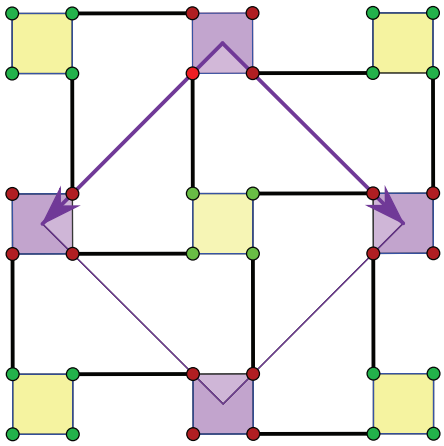

Figure 1. Initial configuration of the planar periodic framework. The displayed fragment is extended by periodicity to an infinite plate-and-bar structure. Two generators of the periodicity lattice are shown as arrows.

Figure 2. Tiles, Ottoman period, Iznik 1560. Harvard Art Museums.

variation, and deployment mechanisms. We rely on a strictly mathematical approach, introduced and developed in previous work [21–25], but the specific treatment of the periodic framework under investigation will be largely self-contained and apt to illustrate the salient points of the general theory.

First, we show that the framework has, with the indicated periodicity, three degrees of freedom. We follow up with the determination of the entire configuration space. Allowing for (controllable) degeneracies, it is the union of three tori of dimension three, with pairwise intersections along tori of dimension two, but no common intersection. Here, and in what follows, a torus of dimension d is the Cartesian product $(S^1)^d$ of a circle S^1 with itself d times.

We focus, then, on the study of what we call “the main locus," which is the torus containing the initial configuration. The other two tori, equivalent under a natural symmetry, are amenable to similar treatment. The key concept, defined after fixing two generators for the periodicity lattice, is the *Gram map*, which associates to a given configuration the corresponding Gram matrix of the two generators. Thus, we have a map with values in the space of 2×2 symmetric matrices $G : (S^1)^3 \to \mathrm{Sym}(2)$, which is most important for understanding the behavior of the framework under deformation and reveals the geometric reasons for auxetic capabilities.

The Gram map may be considered as a periodic analog for the end-effector map in classical robotics and thereby directs our attention to the locus where the differential of the Gram map drops rank, that is, the Jacobian determinant vanishes. This leads to an overall description of the topological behavior of the map.

The abundant possibilities for auxetic one-parameter deformations result from the fact that the differential of the Gram map is generically of maximal rank three. As pointed out in the general setting of [23], auxetic trajectories are analogous to “causal trajectories" in Lorentzian space–times studied in relativity theory and

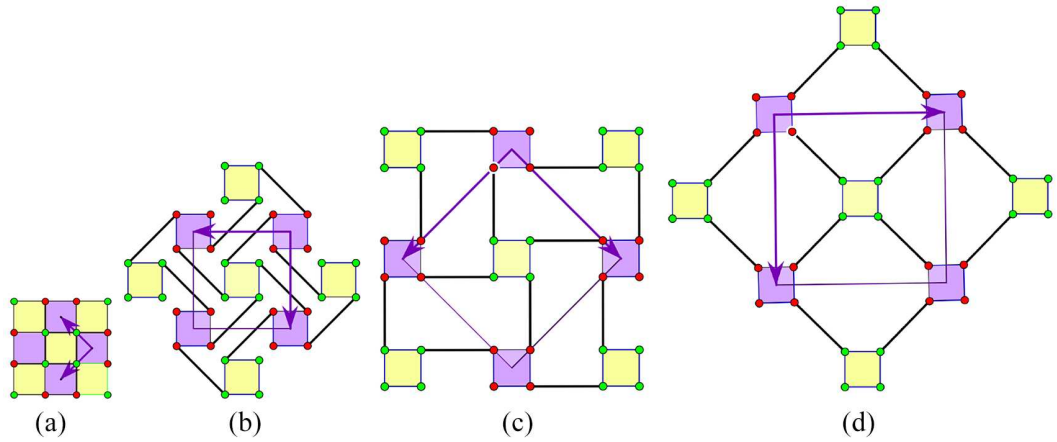

Figure 3. Unfolding stages from tiling to full deployment. From (a) to (c) the deformation is expansive, while from (c) to (d) it is just auxetic.

differential geometry [26]. In the case at hand, we have more than a suggestive analogy, given that the three-dimensional space Sym(2) of symmetric 2×2 matrices has a natural Lorentzian quadratic form or, in other words, Minkowski metric.

Another useful perspective on auxetic behavior results from a comparison with the stronger notion of expansive behavior, which requires that all distances between pairs of vertices increase or stay the same. The region in the parameter space where expansive deformations are possible is more restrictive. At the infinitesimal level (linear approximation), we find, in our case, the contrast between a (quadratic Lorentzian) cone of infinitesimal auxetic deformations, which contains a polyhedral cone of expansive infinitesimal deformations. The extremal rays of this polyhedral cone are very precisely and intuitively described by the possible refinements of the framework to periodic pseudo-triangulations [22, 27].

When we follow the standard deployment trajectory, which unfolds from a tiling configuration to a maximal (unit cell) area configuration, it will be observed that the initial framework lies precisely at the transition point from the expansive part of the trajectory to the still auxetic and area-increasing, but technically non-expansive part of the trajectory, when some pairs of vertices get closer. Figure 3 illustrates these stages. Between the folded (tiling) state and the fully deployed state, the area of the unit cell increases by a factor of $(6 + 4\sqrt{2}) \approx 11.7$.

After the planar investigation, we glance through higher-dimensional versions, with emphasis on the three-dimensional analogous framework, which is related to the crystal structure of Prussian blue [28].

The resulting sequence of sections is as follows: 2. Determination of the configuration space; 3. The Gram map on the main locus; 4. Auxetics and Lorentzian geometry; 5. Expansiveness and pseudo-triangulations; 6. Auxetic deployment: from tiling to maximal area; 7. A glimpse into higher dimensions; 8. Conclusion.

2. Determination of the configuration space

The configuration space of the initial framework is made of all the planar placements of the abstract periodic graph, which preserve the edge length of the squares and their connections, up to equivalence under Euclidean isometries. It can be found by elementary geometrical considerations. We use Figure 4 to describe our setting.

Equivalence under Euclidean isometries can be used to fix a chosen oriented square with center at the origin and vertex ordering 1,2,3,4 as follows: $(-1/2, 1/2)$, $(-1/2, -1/2)$, $(1/2, -1/2)$, $(1/2, 1/2)$. In Figure 4, this is the yellow (light) colored square. The oriented angle at the first vertex from the edge to the fourth vertex and the connection bar to the first purple (dark) colored square is to be denoted by a. This angle is marked in blue (dark) color. Similarly, we have, in order, b, c, and d at the remaining vertices.

The angle expressing the rotation of the purple squares relative to the yellow squares will be denoted by ρ. When translated to a common center, angle ρ is the rotation angle that would bring a purple square over a yellow square (with vertex matching dictated by connections).

Angles are considered modulo 2π, i.e. $a, b, c, d, \rho \in R/2\pi Z \approx S^1$. All bars between squares are of length two, i.e. double the length of a square edge.

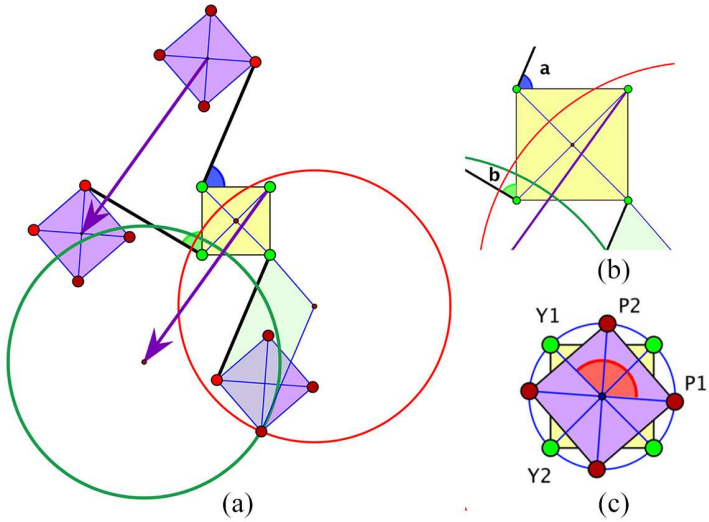

Figure 4. Three marked angles used for the determination of possible configurations: (a) the central square and three of its connections; (b) a close-up with angles a and b; (c) angle ρ. **[AQ: 3]**

In Figure 4, the positions of the first (top) and second purple squares are determined by the given parameters a, b, ρ. The two circles are related to the following constraints. In the third purple square, the vertex connected to $(1/2, -1/2)$ must be on a circle of radius two with that center; hence, the next vertex (counterclockwise) must be on the translated circle shown in red. By periodicity, this vertex, translated to the fourth purple square (not shown) would connect to $(1/2, 1/2)$, hence it belongs to the green circle, which is a circle of radius two, centered at the translate of $(1/2, 1/2)$ by the marked period.

In general, the two circles intersect in two points and the figure shows the placement of the third purple square corresponding to one intersection. This solution is exactly the case when the connecting bar is *parallel* to the first connecting bar and $c = a$ at $(1/2, -1/2)$. This leads to $d = b$ and a full *central symmetry* with respect to the origin. The other solution is distinguished by the fact that the third connecting bar is parallel to the second connecting bar and forms an angle of $c = b - \pi/2$ at $(1/2, -1/2)$. Then the fourth connecting bar must be parallel to the first connecting bar, with an angle of $d = a + \pi/2$ at $(1/2, 1/2)$.

Using the parameters (a, b, c, d, ρ), we can find the coordinates of various elements related to Figure 4. For instance, the center of the first purple square (connected to vertex $(-1/2, 1/2)$) is at

$$C_1 = \left(-\frac{1}{2} + 2\cos a,\ \frac{1}{2} + 2\sin a\right) - \frac{1}{2}(\sin\rho - \cos\rho,\ \sin\rho + \cos\rho) \tag{1}$$

and the center of the purple square connected to $(-1/2, -1/2)$ is at

$$C_2 = \left(-\frac{1}{2} - 2\sin b,\ -\frac{1}{2} + 2\cos b\right) + \frac{1}{2}(\sin\rho + \cos\rho,\ -\sin\rho + \cos\rho) \tag{2}$$

The center of the fourth purple square would be at

$$C_4 = \left(\frac{1}{2} + 2\sin d,\ \frac{1}{2} - 2\cos d\right) - \frac{1}{2}(\sin\rho + \cos\rho,\ -\sin\rho + \cos\rho) \tag{3}$$

resulting in the following expressions for the two generators of the periodicity lattice:

$$\lambda_1 = C_2 - C_1 = (\sin\rho - 2\cos a - 2\sin b,\ -1 + \cos\rho - 2\sin a + 2\cos b) \tag{4}$$

$$\lambda_2 = C_4 - C_1 = (1 - \cos\rho - 2\cos a + 2\sin d,\ \sin\rho - 2\sin a - 2\cos d). \tag{5}$$

This preliminary inquiry shows that, for a description of the configuration space of the initial framework, we should allow at first the full range S^1 of the angle parameters and eliminate afterwards the degeneracy locus

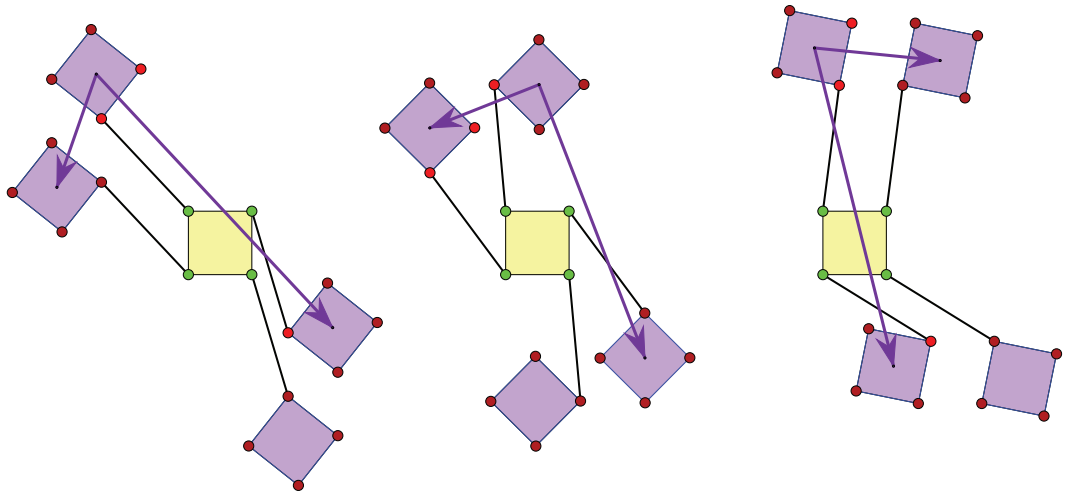

Figure 5. The three types of possible configurations. Type (ii), in the middle, has central symmetry with respect to the midpoint of the yellow square. Types (i) and (iii) are exchanged by a reflection in a diagonal of the yellow square.

where the generators of the periodicity lattice become linearly dependent. We note that configurations with self-crossings are *allowed* and participate in the makeup of our result.

By exploiting the parallelisms noticed previously, we obtain a natural compactification of the configuration space as a union of *three tori of dimension three*, corresponding to the following three types of configuration:

(i) The first two connecting bars are parallel and the last two connecting bars are parallel, with conditions

$$b = a - \frac{\pi}{2} \qquad \text{and} \qquad d = c - \frac{\pi}{2} \tag{6}$$

(ii) The first and third connecting bars are parallel and the second and fourth connecting bars are parallel (with central symmetry at the origin), with conditions

$$c = a \qquad \text{and} \qquad d = b \tag{7}$$

(iii) The first and fourth connecting bars are parallel and the second and third connecting bars are parallel, with conditions

$$b = c + \frac{\pi}{2} \qquad \text{and} \qquad d = a + \frac{\pi}{2} \tag{8}$$

Remark. The three tori $(S^1)^3 \subset (S^1)^5$ corresponding to these types do intersect in pairs (along two tori) but do not have a common intersection.

$$\text{(i)} \cap \text{(ii)}: \qquad b = d = a - \frac{\pi}{2}, \qquad c = a \tag{9}$$

$$\text{(ii)} \cap \text{(iii)}: \qquad b = d = a + \frac{\pi}{2}, \qquad c = a \tag{10}$$

$$\text{(iii)} \cap \text{(i)}: \qquad b = a + \frac{3\pi}{2}, \qquad c = a + \pi, \qquad d = a + \frac{\pi}{2} \tag{11}$$

Examples of configurations belonging to each type are shown in Figure 5.

2.1. Action of the dihedral group D_8

The dihedral group of order eight D_8 is the symmetry group of a square and has a natural action on the configuration space and its compactification, as described previously. It is enough to indicate the action on the

parameters (a, b, c, d, ρ) of the two involutions s_1 and s_2, corresponding to reflection on the vertical axis and reflection in the diagonal through vertex one. We find:

$$s_1(a, b, c, d, \rho) = \left(\frac{3\pi}{2} - d,\ \frac{3\pi}{2} - c,\ \frac{3\pi}{2} - b, \frac{3\pi}{2} - a,\ -\rho\right) \tag{12}$$

$$s_2(a, b, c, d, \rho) = \left(\frac{3\pi}{2} - a,\ \frac{3\pi}{2} - d,\ \frac{3\pi}{2} - c, \frac{3\pi}{2} - b,\ -\rho\right) \tag{13}$$

Since s_2 exchanges types (i) and (iii), it suffices to examine types (ii) and (iii). We pursue type (ii) and call the torus $(S^1)^3$ parametrized by $(a, b, \rho) \in R/2\pi Z \approx S^1$ the *main locus*, with the initial configuration at $(a, b, \rho) = (\pi/2, \pi/2, -\pi/2)$. Similar considerations apply to type (iii).

The main locus is invariant under the action of D_8, with central symmetry inducing the identity. Thus, the effective action is that of a *Klein group* with four elements. Abstractly, the stabilizer subgroup of type (iii) is also a Klein group with four elements.

3. The Gram map on the main locus

The main locus was defined as the three-dimensional torus compactification of configurations of type (ii), that is, the locus cut out by equation (7), making $c = a$ and $d = b$, in the five-dimensional torus $(S^1)^5$ parametrized by (a, b, c, d, ρ). We use parameters (a, b, ρ) for this locus.

3.1. Basic formulas

3.1.1. Periods. Since $d = b$, equations (4) and (5) give

$$\lambda_1(a, b, \rho) = (\sin\rho - 2\cos a - 2\sin b,\ -1 + \cos\rho - 2\sin a + 2\cos b) \tag{14}$$

$$\lambda_2(a, b, \rho) = (\ 1 - \cos\rho - 2\cos a + 2\sin b,\ \sin\rho - 2\sin a - 2\cos b) \tag{15}$$

3.1.2. Gram matrix entries. The Gram matrix $G(\lambda_1, \lambda_2)$ associated to these two generators of the periodicity lattice is a 2×2 symmetric matrix with the following entries:

$$\begin{aligned}\lambda_{11}(a, b, \rho) &= \langle\lambda_1, \lambda_1\rangle \\ &= 10 - 2\cos\rho - 8\sin(a - b) + 4[(\sin a - \cos b) - (\sin(a + \rho) - \cos(b + \rho))]\end{aligned} \tag{16}$$

$$\begin{aligned}\lambda_{12}(a, b, \rho) &= \lambda_{21}(a, b, \rho) \\ &= \langle\lambda_1, \lambda_2\rangle = 2\sin\rho[(\sin b + \cos b) - (\sin a + \cos a)] + 2(1 - \cos\rho)[(\sin a - \cos a) - (\sin b - \cos b)]\end{aligned} \tag{17}$$

$$\begin{aligned}\lambda_{22}(a, b, \rho) &= \langle\lambda_2, \lambda_2\rangle \\ &= 10 - 2\cos\rho + 8\sin(a - b) + 4[(\sin b - \cos a) - (\sin(b + \rho) - \cos(a + \rho))]\end{aligned} \tag{18}$$

3.1.3. Oriented unit cell area. The parallelogram with vector edges λ_1 and λ_2 is a fundamental domain (*unit cell*) for the action of the periodicity lattice. From equations (14) and (15), we find

$$\mathcal{A}(a, b, \rho) = 8\cos(a - b) - 2\sin\rho\,(\sin a + \sin b + \cos a + \cos b) + (2 - 2\cos\rho)(1 + \sin a + \sin b - \cos a - \cos b). \tag{19}$$

3.2. Critical points of the area function

The critical points of $\mathcal{A} : (S^1)^3 \to R$ are given by the vanishing of the gradient

$$\begin{aligned}
\nabla\mathcal{A}(a,b,\rho) &= \left(\frac{\partial\mathcal{A}}{\partial a}, \frac{\partial\mathcal{A}}{\partial b}, \frac{\partial\mathcal{A}}{\partial \rho}\right) = 0 \\
\frac{\partial\mathcal{A}}{\partial a} &= 8\sin(b-a) - 2\sin\rho\,(\cos a - \sin a) + (2 - 2\cos\rho)(\cos a + \sin a) \\
\frac{\partial\mathcal{A}}{\partial b} &= -8\sin(b-a) - 2\sin\rho\,(\cos b - \sin b) + (2 - 2\cos\rho)(\cos b + \sin b) \\
\frac{\partial\mathcal{A}}{\partial \rho} &= -2\cos\rho\,(\cos a + \sin a + \cos b + \sin b) + 2\sin\rho\,(1 + \sin a - \cos a + \sin b - \cos b)
\end{aligned} \tag{20}$$

The system (equation (20)) leads to:

$$\frac{1}{2}\left(\frac{\partial\mathcal{A}}{\partial a} + \frac{\partial\mathcal{A}}{\partial b} - \frac{\partial\mathcal{A}}{\partial \rho}\right) = -\sin\rho + (\cos a + \sin a + \cos b + \sin b) = 0 \tag{21}$$

$$\frac{1}{2}\cdot\frac{\partial\mathcal{A}}{\partial \rho} = \sin\rho\,(1 - \cos\rho + \sin a - \cos a + \sin b - \cos b) = 0 \tag{22}$$

We find the following solutions:

$$\rho = 0 \quad \text{and} \quad a - b = 0 \quad \text{mod } (2\pi) \tag{23}$$

$$\rho = 0 \quad \text{and} \quad a - b = \pi \quad \text{mod } (2\pi) \tag{24}$$

$$\rho = \pi \quad \text{and} \quad a = \frac{\pi}{4} \pm \frac{\pi}{2}, \quad b = \frac{\pi}{4} \pm \frac{\pi}{2} \quad \text{mod } (2\pi) \tag{25}$$

The maximum is reached for $(a, b, \rho) = (3\pi/4, 3\pi/4, \pi)$, with

$$\mathcal{A}(3\pi/4, 3\pi/4, \pi) = 8 + 4(1 + 2\sqrt{2}) = 12 + 8\sqrt{2} \tag{26}$$

and the minimum is obtained at all points of the one-torus (equation (24)), with

$$\mathcal{A}(a, a - \pi, 0) = -8 \tag{27}$$

The tiling configuration $(0, 0, \pi/2)$ has a (unit cell) area $\mathcal{A}(0, 0, \pi/2) = 2$, hence *from tiling to maximal deployment* the area increases $(6 + 4\sqrt{2}) \approx 11.7$ times.

There is no critical point on the area vanishing locus $\mathcal{A} = 0$; hence, this locus is a *smooth surface*. It has two connected components, as shown in Figure 6. The complement $(S^1)^3 \setminus \{\mathcal{A} = 0\}$ has two connected components, corresponding to $\mathcal{A} > 0$ and $\mathcal{A} < 0$.

3.2.1. Three involutions. As already noted, restricting the action of the dihedral group D_8 to the main locus yields an effective action of a Klein group. Involutions are labeled:

$$\begin{aligned}
\iota_1(a,b,\rho) &= (b, a, \rho) \\
\iota_2(a,b,\rho) &= (-(a + \pi/2), -(b + \pi/2), -\rho) \\
\iota_3(a,b,\rho) &= (-(b + \pi/2), -(a + \pi/2), -\rho)
\end{aligned}$$

The three involutions commute with one another and generate a group with four elements $K = \{id, \iota_1, \iota_2, \iota_3\}$. We have

$$\iota_1\lambda_1(a,b,\rho) = \lambda_1(\iota_1(a,b,\rho)) = \lambda_1(b,a,\rho) = -\lambda_2(a,b,\rho)^{\perp} \tag{28}$$

where $(u, v)^{\perp} = (-v, u)$ is the rotation with $\pi/2$.

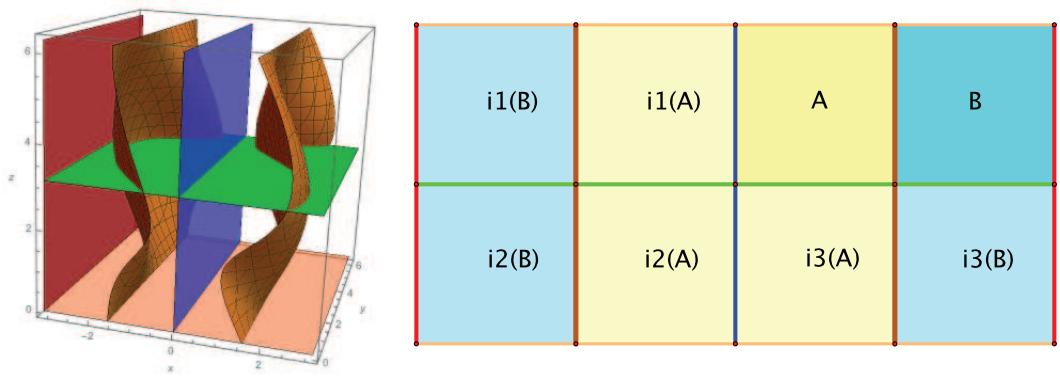

Figure 6. Schematic action of involutions on the partition of $(S^1)^3$ determined by the vanishing Jacobian determinant locus. Yellow hue for $\mathcal{A} > 0$ and blue for $\mathcal{A} < 0$.

The involution ι_1 acts on Gram matrices by

$$\iota_1(G) = \begin{pmatrix} \lambda_{22} & -\lambda_{12} \\ -\lambda_{12} & \lambda_{11} \end{pmatrix} \tag{29}$$

Similar computations for ι_2 and $\iota_3 = \iota_1 \circ \iota_2$ show that

$$\iota_2(G) = \begin{pmatrix} \lambda_{22} & \lambda_{12} \\ \lambda_{12} & \lambda_{11} \end{pmatrix} \tag{30}$$

$$\iota_3(G) = \begin{pmatrix} \lambda_{11} & -\lambda_{12} \\ -\lambda_{12} & \lambda_{22} \end{pmatrix} \tag{31}$$

Note that all three involutions keep the oriented area function unchanged and take each connected component of the configuration space $(S^1)^3 \setminus \{\mathcal{A} = 0\}$ to itself. The involutions ι_1 and ι_2 exchange the two connected components of the vanishing area locus. The point of maximal deployment $(3\pi/4, 3\pi/4, \pi)$ is invariant.

3.3. The Gram map

We consider $G : (S^1)^3 \to \mathrm{Sym}(2)$ as a map $(a, b, \rho) \mapsto G(a, b, \rho)$ from three variables $a, b, \rho \pmod{2\pi}$ to three variables $\lambda_{11}, \lambda_{12}, \lambda_{22}$, which give the entries of the symmetric matrix $G(a, b, \rho)$. The differential of this map is singular when the Jacobian determinant vanishes and this occurs on the locus

$$\det(\mathrm{d}G(a, b, \rho)) = \mathcal{A}(a, b, \rho) \sin(a - b) \sin \rho = 0 \tag{32}$$

As a result of the two other factors, each of the two connected components of the configuration space $(S^1)^3 \setminus \{\mathcal{A} = 0\}$ is subdivided into four open regions where G is locally invertible. The map G is *equivariant* with respect to the action of the Klein group K described, that is:

$$G(\iota_k(a, b, \rho)) = \iota_k(G(a, b, \rho)), \qquad k = 1, 2, 3 \tag{33}$$

Moreover, K takes to itself each of the following loci: $\mathcal{A} = 0$, $a - b = 0 \mod 2\pi$, $a - b = \pi \mod 2\pi$, $\rho = 0 \mod 2\pi$, and $\rho = \pi \mod 2\pi$.

For visual purposes, we may favor new coordinates $x = a - b$, $y = b$, $z = \rho$ on $(S^1)^3$. Then we obtain Figure 6 for the partition determined by the vanishing Jacobian determinant locus (32) in $(S^1)^3$:

$$\begin{pmatrix} x \\ y \\ z \end{pmatrix} = \begin{pmatrix} 1 & -1 & 0 \\ 0 & 1 & 0 \\ 0 & 0 & 1 \end{pmatrix} \begin{pmatrix} a \\ b \\ \rho \end{pmatrix} \tag{34}$$

The degeneracy (vanishing area) locus is shown in brown and separates (borders) the two connected components of the configuration space. The faces $z = 0, 2\pi$ and $x = \pm\pi$ of the represented unit cell are also in

the vanishing Jacobian determinant locus. Topologically, the complement of this locus in $(S^1)^3$ is made of eight disjoint *open solid rings*.

The involution $\iota_1(x, y, z) = (-x, x + y, z)$ pairs the four rings "above" the green 2-torus ($z = \pi$) and likewise the four rings "below." If we represent schematically the eight open solid rings in the complement of the vanishing Jacobian determinant locus, as in Figure 6, we see that symmetry under the action of the Klein group K reduces the study of G to just two representative solid rings and their boundaries.

The region marked A stands for the connected component bounded by $\rho = 0 \mod 2\pi$, $a - b = 0 \mod (2\pi)$, $\rho = \pi \mod (2\pi)$, and a piece belonging to one connected component of $\mathcal{A} = 0$.

The region marked B is separated from A by the common boundary contained in $\mathcal{A} = 0$ (with $\mathcal{A} > 0$ in A and $\mathcal{A} < 0$ in B), with the remaining of its boundary contained in $\rho = \pi \mod (2\pi)$, $a - b = \pi \mod (2\pi)$, and $\rho = 0 \mod (2\pi)$.

3.4. The Gram map on the vanishing Jacobian locus

The vanishing Jacobian locus (equation (32)) consists of several surfaces where the differential of the Gram map has rank less than three. Following G on these surfaces will disclose the global topological behavior of the Gram map and lead to a fairly detailed understanding of its image.

The 2-torus $z = \rho = 2\pi \equiv 0$ (corresponding to the identified "top" and "bottom" faces of the unit cell shown in Figure 6) gives Gram matrices with

$$\lambda_{11}(a, b, 0) = 8(1 - \sin(a - b)), \qquad \lambda_{12} = 0, \qquad \lambda_{22}(a, b, 0) = 8(1 + \sin(a - b))$$

hence the Gram map image for $\rho = 0$ is the segment with $\lambda_{11}, \lambda_{22} \geq 0$ of the line

$$\lambda_{11} + \lambda_{22} = 16, \qquad \lambda_{12} = 0. \tag{35}$$

with endpoints at

$$\begin{pmatrix} 16 & 0 \\ 0 & 0 \end{pmatrix} \qquad \text{and} \qquad \begin{pmatrix} 0 & 0 \\ 0 & 16 \end{pmatrix}.$$

The blue 2-torus $a = b \pmod{2\pi}$, in the positive area connected component of $(S^1)^3 \setminus \{\mathcal{A} = 0\}$, is point-invariant under the involution ι_1 and maps by G to a segment in $R_+ \cdot I_2$. We have $\lambda_{11} = \lambda_{22}$, $\lambda_{12} = 0$, with

$$\lambda_{11}(a, a, \rho) = 10 - 2\cos\rho + 4[(\sin a - \cos a) - (\sin(a + \rho) - \cos(a + \rho))]$$

In particular

$$\lambda_{11}(a, a, 0) = 8$$

and

$$\lambda_{11}(a, a, \pi) = 12 + 8(\sin a - \cos a).$$

The resulting image $G(a, a, \rho)$ is the segment

$$\left[12 - 8\sqrt{2}, 12 + 8\sqrt{2}\right] \cdot I_2. \tag{36}$$

In the negative area connected component, the 2-torus $a - b = \pi \pmod{2\pi}$ (corresponding to the identified "left" and "right" faces of the unit cell shown in Figure 6) maps to matrices $G(a, a + \pi, \rho)$ with trace and determinant depending only on $\cos\rho$:

$$\lambda_{11} + \lambda_{22} = \operatorname{Tr} G(a, a + \pi, \rho) = 4(5 - \cos\rho) \tag{37}$$

$$\mathcal{A}(a, a + \pi, \rho) = -2(3 + \cos\rho), \qquad \det(G) = \mathcal{A}^2 \tag{38}$$

Elimination of ρ leads to the equation in Gram coordinates of the *quadric* containing this image:

$$(\lambda_{11} - \lambda_{22})^2 + 2^2\lambda_{12}^2 - 2^6(\lambda_{11} + \lambda_{22}) + 2^{10} = 0. \tag{39}$$

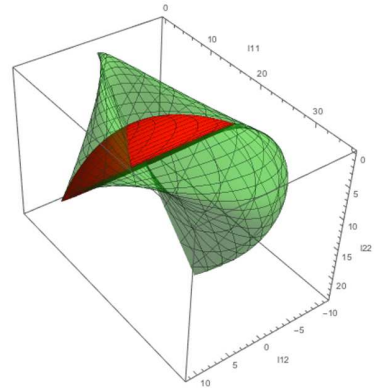

Figure 7. $G(a, b, \pi), 0 \leq a - b \leq \pi$, and the "red cap" surface $G(a, a + \pi, \rho)$.

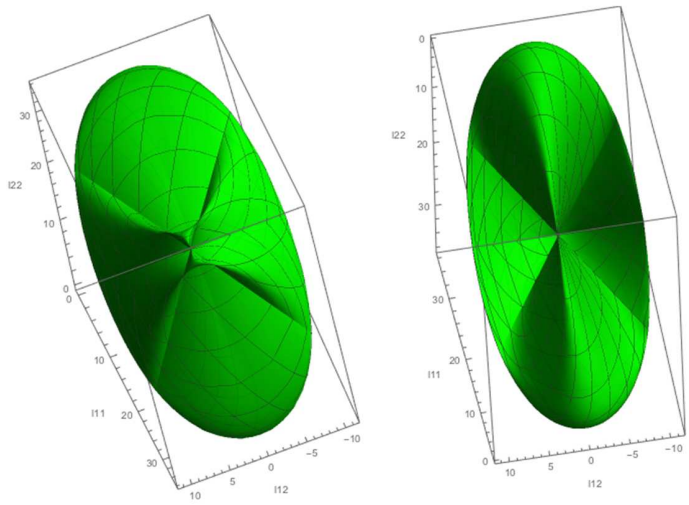

Figure 8. Two views of the locus $G(a, b, \pi)$, $a, b \in [0, 2\pi]$, with emphatic Klein group symmetry: from the side of the origin and then from the other side.

The image locus $G(a, a + \pi, \rho)$ appears in Figure 7 as a *cap* on the paraboloid of revolution (equation (39)) with axis $R \cdot I_2$. This axis is intersected for $\rho = 0$ at $8I_2$ and the line (equation (35)) is tangent to the paraboloid at this same point $8I_2$. The image remains bounded by the plane $\lambda_{11} + \lambda_{22} = 24$.

The more intriguing green surface in Figure 7 is the image $G(a, b, \pi)$, for $0 \leq a - b \leq \pi$. For the full range, $-\pi \leq a - b \leq \pi$, one has to imagine the union with $G(\iota_1(a, b, \pi)) = G(b, a, \pi)$, which is obtained by rotation with π around the axis $R \cdot I_2$. Renditions with manifest K symmetry are given in Figure 8. As before, the algebraic equation of the surface containing this union locus can be obtained by an elimination process.

The outcome is a *sextic surface* in Gram coordinates $\lambda_{11}, \lambda_{12}, \lambda_{22}$. Using the polynomials $s = \lambda_{11} + \lambda_{22}$, $p = \lambda_{11}\lambda_{22}$, and $q = \lambda_{12}^2$, which are invariant under the action of the Klein group, the sextic takes the following form:

$$\begin{aligned}&\left(16384q - 16384p + 4096p^2 + 10240pq + 2048q^2 - 64pq^2 + 64q^3\right)\\&\quad + \left(16384p - 1024pq\right)s + \left(4096 - 5632p - 3072q + 32pq - 16q^2\right)s^2\\&\qquad + \left(-4096 + 256p + 256q\right)s^3 + \left(1152 - 4p - 4q\right)s^4 - 64s^5 + s^6 = 0 \quad (40)\end{aligned}$$

The coefficients have simple expressions in powers of two: $16,384 = 2^{14}$, $4096 = 2^{12}$, $10,240 = 2^{13} + 2^{11}$, $2048 = 2^{11}$, $64 = 2^6$, $1024 = 2^{10}$, $5632 = 2^{12} + 2^{10} + 2^9$, $3072 = 2^{11} + 2^{10}$, $256 = 2^8$, $1152 = 2^{10} + 2^7$.

For a more detailed understanding of this sextic surface, it is useful to note the presence of *five concurrent singular lines*: the conspicuous axis $R \cdot I_2$ and another four lines through $4I_2$:

$$\lambda_{11} = 4, \qquad 2\lambda_{12} = \lambda_{11} - \lambda_{22} \tag{41}$$
$$\lambda_{11} = 4, \qquad 2\lambda_{12} = \lambda_{22} - \lambda_{11} \tag{42}$$
$$\lambda_{22} = 4, \qquad 2\lambda_{12} = \lambda_{11} - \lambda_{22} \tag{43}$$
$$\lambda_{22} = 4, \qquad 2\lambda_{12} = \lambda_{22} - \lambda_{11} \tag{44}$$

These lines support the following image segments:

$$G\left(\frac{3\pi}{2}, b, \pi\right), \qquad G(a, 0, \pi), \qquad G\left(a, \frac{3\pi}{2}, \pi\right), \qquad G(0, b, \pi). \tag{45}$$

The hyperbola

$$\lambda_{11} = \lambda_{22},\ \lambda_{11}\lambda_{22} - \lambda_{12}^2 = 16 \tag{46}$$

is also singular on the sextic surface.

Last but not least, we take note of the image of the degeneracy locus given by the vanishing of the area function (equation (19)). Since $\det(G) = \mathcal{A}^2$, this locus is contained in the quadratic cone

$$\lambda_{11}\lambda_{22} - \lambda_{12}^2 = 0 \tag{47}$$

The entire image $G((S^1)^3)$ is a compact subset in the positive semidefinite cone of Sym(2), with the latter cone bounded by half of equation (47). We'll see in Section 4 that *auxetic trajectories* can be defined and conveniently explored in terms of the Lorentzian geometry of Sym(2), with equation (47) as the *light cone*.

3.5. Image and bounding planes

On account of the previous developments, we can proceed with a more detailed description of the image $G((S^1)^3)$ and its boundary. The center of attention is the algebraic surface of degree six given by equation (40).

3.5.1. The contact curve. We determine first the *contact curve* given by degenerate configurations contained in the intersection of the sextic surface (equation (40)) with the cone (equation (47)). More precisely, we find the Gram image of the two loops in the 2-torus $\rho = \pi$ where the area vanishes. Elimination of a and b in the system of equations (16) to (18) and $\mathcal{A} = 0$, written for $\rho = \pi$, leads to a rather simple cubic companion for the cone's equation, namely

$$s^3 - 2^5 s^2 + 2^6 s - 2^2 sq + 2^7 q = 0, \tag{48}$$

where $s = \lambda_{11} + \lambda_{22}$, $q = \lambda_{12}^2$. This allows a direct recognition of the contact curve as part of the real space sextic defined by the intersection of equations (48) and (47). The two connected components are exchanged by ι_1, as can be seen in Figure 9.

Remark. To relate, visually and topologically, the domain and the image of the Gram map, the following observations on *crossing and brushing* may be useful. In the domain $(S^1)^3$, a general *crossing* of one or the other connected component of the surface $\mathcal{A} = 0$ corresponds via G to *brushing*, i.e. touching tangentially the "light cone" $\det(G) = 0$, while remaining inside. Similarly, a general crossing of the 2-torus $a - b = \pi \pmod{2\pi}$ in $(S^1)^3$ corresponds to brushing the "cap" surface $G(a, a + \pi, \rho)$.

Accordingly, one expects the contact curve to be along a tangency locus between the sextic surface supporting $G(a, b, \pi)$ and the light cone. This is confirmed algebraically by the fact that, for $\det(G) = p - q = 0$, making $p = q$ in the sextic polynomial (equation (40)) yields precisely the square of the cubic polynomial (equation (48)).

The paraboloid (equation (39)) also intersects tangentially the light cone (equation (47)) along a (double) circle in the plane $\mathrm{Tr}(G) = \lambda_{11} + \lambda_{22} = 2^5$, but this intersection is beyond the cap surface $G(a, a + \pi, \rho)$.

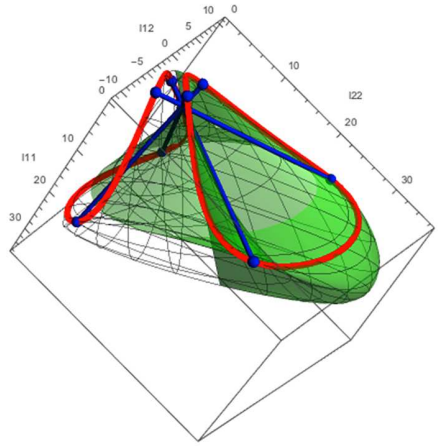

Figure 9. The contact curve between the light cone and the Gram image supported in the sextic surface is marked in red. Part of the sextic is rendered as only a mesh outline. The four segments are given in equation (45).

3.5.2. A convex encasement of the image. The position of $G((S^1)^3)$ in the *positive semidefinite cone* of Sym(2) can be delineated more sharply by exploiting the *projective geometry* of the sextic surface (equation (40)). When we look at the *sextic curve at infinity* corresponding to our affine equation, that is, when we retain the *homogeneous part* of total degree six in $\lambda_{11}, \lambda_{12}, \lambda_{22}$ of equation (40), we find that the corresponding *curve at infinity*, written in homogeneous coordinates $(\lambda_{11} : \lambda_{12} : \lambda_{22}) \in P_2$, decomposes into two double lines and a conic, namely

$$(\lambda_{11} + 2\lambda_{12} + \lambda_{22})^2(\lambda_{11} - 2\lambda_{12} + \lambda_{22})^2 \left[(\lambda_{11} - \lambda_{22})^2 + 4\lambda_{12}^2\right] = 0 \tag{49}$$

For our affine sextic surface, this information at infinity signals the privileged role of projective planes passing through the double lines in equation (49) and a particular significance for the projection with direction $(1 : 0 : -1)$, given by the point of intersection of the two lines. Moreover, we may observe that the only real point of the quadratic factor in equation (49) is $(1 : 0 : 1)$, which is the point at infinity of the axis $R \cdot I_2$. The precise outcome is the following.

Theorem 1. *Let* $\lambda_{11}, \lambda_{12}, \lambda_{22}$ *be coordinates for* Sym(2). *Each of the four affine planes*

$$\lambda_{11} + 2\lambda_{12} + \lambda_{22} = 24 + 16\sqrt{2} \tag{50}$$

$$\lambda_{11} - 2\lambda_{12} + \lambda_{22} = 24 + 16\sqrt{2} \tag{51}$$

$$\lambda_{11} + 2\lambda_{12} + \lambda_{22} = 24 - 16\sqrt{2} \tag{52}$$

$$\lambda_{11} - 2\lambda_{12} + \lambda_{22} = 24 - 16\sqrt{2} \tag{53}$$

meets the sextic surface (equation (40)*) tangentially along an ellipse. The entire image* $G((S^1)^3)$ *is on the side of* $4I_2$ *for the respective closed half-spaces. The intersection of the positive semidefinite cone in* Sym(2) *with these four half-spaces provides a compact convex encasement of* $G((S^1)^3)$.

We leave out the straightforward computational verifications in favor of some additional remarks. The planes described by equations (50) to (53) will be called *bounding planes*.

The configuration part of the sextic surface is shown in Figure 10 as seen "from the point at infinity" $(1 : 0 : -1)$, that is, along the vector direction

$$\begin{pmatrix} 1 & 0 \\ 0 & -1 \end{pmatrix},$$

shared by the four bounding planes. Projecting on the plane $\lambda_{11} = \lambda_{22}$, yields the nearby planar rendition, which includes the image of the contact curve.

The vertices of the rhombus are $(12 \pm 8\sqrt{2})I_2$ and

$$\begin{pmatrix} 12 & \pm 8\sqrt{2} \\ \pm 8\sqrt{2} & 12 \end{pmatrix},$$

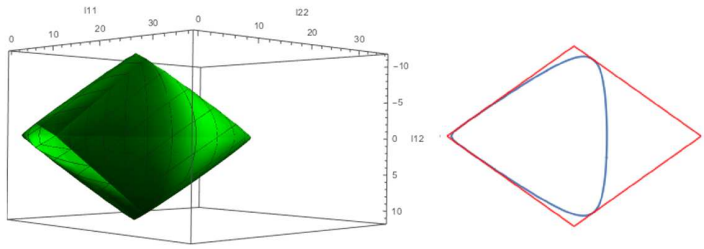

Figure 10. A particular perspective on the locus $G(a, b, \pi)$, $a, b \in [0, 2\pi]$, which takes advantage of the two pairs of planes passing through the double lines of the projective sextic surface at infinity. Planar projection on $\lambda_{11} = \lambda_{22}$ includes projection of the contact curve.

that is, the endpoints of the axis segment (equation (36)) and the endpoints of the hyperbola arc supported by equation (46).

On each bounding plane, there are four points related to the singularity curves of the sextic surface mentioned in equations (41) to (46). For instance, the plane of equation (50) passes through the maximal area point, one endpoint of the hyperbola arc and two endpoints of segments supported by the lines of equations (42) and (43), which belong to the contact curve as well. The latter points are

$$\begin{pmatrix} 4 & 4+4\sqrt{2} \\ 4+4\sqrt{2} & 12+8\sqrt{2} \end{pmatrix}, \qquad \begin{pmatrix} 12+8\sqrt{2} & 4+4\sqrt{2} \\ 4+4\sqrt{2} & 4 \end{pmatrix}. \tag{54}$$

These two points have the same projection on $\lambda_{11} = \lambda_{22}$, namely

$$\begin{pmatrix} 8+4\sqrt{2} & 4+4\sqrt{2} \\ 4+4\sqrt{2} & 8+4\sqrt{2} \end{pmatrix} \tag{55}$$

which accounts for one of the tangency points perceptible in Figure 10 between the projection of the contact curve and the projection of the bounding planes.

3.5.3. Another involution on the sextic surface. In view of the paramount role of the sextic surface (equation (40)) for understanding the range of the Gram map, we point out the existence of another *involution*, perhaps less noticeable visually, but natural in the context of projective geometry.

If we run a generic line through the *singular point* $4I_2$, the restriction of the sextic will have a zero of multiplicity four at this point and one can define an *involution* on a dense open subset of the sextic surface by exchanging the two remaining roots. Equivalently, projection from $4I_2$ on the projective plane at infinity represents the surface as a branched double covering of P_2 and the involution exchanges the two sheets of this covering.

In particular, this additional symmetry explains the resemblance between the region around the "lower end" of the axis segment and the region around the "upper end."

4. Auxetics and Lorentzian geometry

The notion of *auxetic behavior* emerged in materials science and refers to structural deformations exhibiting lateral widening on directional stretching [29–32]. A purely geometric approach for periodic frameworks was introduced in [23], leading to a general mathematical solution of the structure and design problem [24]. For the periodic framework of interest in this paper, a strictly mathematical treatment is both a necessity and an advantage.

With the background material on the Gram map covered previously, it will be readily apparent that geometric auxetics for our framework amount to Lorentzian geometry in Sym(2). This is due to the already noticed fact that the *positive semidefinite cone* in Sym(2) is bounded by the *light cone* $\det(G) = 0$. The quadratic form $\det(G) = \lambda_{11}\lambda_{22} - \lambda_{12}^2$ has signature $(1, 2)$ and Lorentzian geometry is special relativity (i.e. flat pseudo-Riemannian geometry) for the three-dimensional *"space–time"* Sym(2) endowed with this quadratic form.

The key notion of geometric auxetics, in arbitrary dimension [23], is the following.

Definition 1. *A differentiable one-parameter deformation of a periodic framework is auxetic when the associated curve given by the Gram map (for periodicity generators) has all its velocity vectors in the positive semidefinite cone.*

Thus, for two-dimensional periodic frameworks, an auxetic deformation path corresponds through the Gram map with a *causal line* in Sym(2) and this is the criterion used in the present work.

Theorem 2. *Any framework configuration where the differential of the Gram map has maximal rank three allows local auxetic deformations.*

This follows directly from Definition 1 and our description of the configuration space in Section 2. On the main locus, we have maximal rank on the complement of the vanishing Jacobian locus. For any configuration (a, b, ρ) in this complement, the choice of a local causal trajectory through $G(a, b, \rho)$ provides, by the existence of a local inverse of G, an auxetic deformation path in a neighborhood of (a, b, ρ) in the configuration space.

Remark. If we consider the Gram map as the *direct kinematics* of a periodic framework, the design of auxetic deformations appears as an exercise in *inverse kinematics*. The simplest causal trajectories in Sym(2) are segments along lines with direction vector inside the light cone. In our setting, a conspicuous instance is the axis segment identified in equation (36). This is the source of the auxetic deformation called *the standard deployment* and examined more closely in Section 6.

5. Expansiveness and pseudo-triangulations

The previous section has shown that the three degrees of freedom of our periodic framework and a generically immersive Gram map bring about a profusion of possibilities for auxetic one-parameter deformations. Selecting a particular trajectory requires some form of control or additional constraints for reduction to a single degree of freedom.

We discuss this concern in connection with the notion of *expansive behavior*, which implies *auxetic behavior*. The stronger condition of expansiveness for a one-parameter deformation of a periodic framework requires that all distances between pairs of vertices increase or stay the same. In dimension two, the essence of expansive behavior is captured in the concept of *periodic pseudo-triangulation* [22, 27].

Definition 2. *A pseudo-triangle is a simple planar polygon with exactly three interior angles smaller than π.*

Definition 3. *A planar periodic pseudo-triangulation is a non-crossing periodic framework, which is pointed at every vertex (i.e. all edges adjacent to a vertex are on one side of some line through that vertex) and tiles the plane with pseudo-triangles.*

In Figure 11, we show that certain configurations in the main locus can be refined to periodic pseudo-triangulations. The squares are represented as triangulated by a diagonal in order to operate in terms of bar-and-joint frameworks. Up to periodicity, there are two octagonal faces. When, a refinement to a pseudo-triangulation exists, there are actually four of them, as illustrated. These refinements correspond with the extremal rays of the *cone of expansive infinitesimal deformations* of the given configuration. A refinement needs two additional edge orbits, which eliminate two degrees of freedom.

Remark. The convex hull of a pseudo-triangle is a triangle. The basic theory of periodic pseudo-triangulations is presented in [22], including the fact that they have one degree of freedom and deform expansively as long as they remain periodic pseudo-triangulations (and parametrization is in the sense of increased distances).

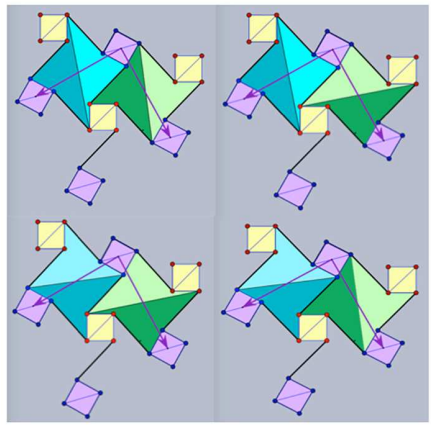

Figure 11. Refinements to pseudo-triangulations.

6. Auxetic deployment: from tiling to maximal area

We can examine now a quite remarkable one-parameter path in the deformation space of our framework: *the standard deployment and refolding*. With $a \in [0, 3\pi/2]$ as parameter, we have:

$$\begin{aligned}
\text{tiling configuration:} &\quad (0, 0, \pi/2),\\
\text{deployment trajectory:} &\quad \left(a, a, \frac{\pi}{2} - 2a\right), a \in [0, 3\pi/4],\\
\text{maximal area configuration:} &\quad (3\pi/4, 3\pi/4, \pi),\\
\text{folding trajectory:} &\quad \left(a, a, \frac{\pi}{2} - 2a\right), a \in [3\pi/4, 3\pi/2],\\
\text{new tiling configuration:} &\quad (3\pi/2, 3\pi/2, -\pi/2).
\end{aligned}$$

There is no self-intersection in the open interval $(0, 3\pi/2)$. The Gram image $G(a, a, \pi/2 - 2a)$ covers the axis segment $[2, 12 + 8\sqrt{2}]I_2$, once in deployment, for $a \in [0, 3\pi/4]$ and once again in refolding, for $a \in [3\pi/4, 3\pi/2]$.

For $a \in (0, \pi/2)$, the deployment is expansive, since faces allow refinements to periodic pseudo-triangulations and, infinitesimally, the deformation is in the expansive cone. However, beyond $a = \pi/2$, the deployment is just auxetic, with the unit cell area continuing to increase toward the maximum, but with certain pairs of vertices getting closer in the process.

Configurations for $a = 0, \pi/4, \pi/2$, and $3\pi/4$ are shown in Figure 3. The deformation path is fixed by ι_1, while transforming by ι_2 and ι_3 amounts to running in reverse. The configuration of full deployment has highest crystallographic symmetry, including an enhanced periodicity allowing the translation of yellow squares over purple squares [33].

7. A glimpse into higher dimensions

A natural analog for the high symmetry configuration can be imagined in arbitrary dimension d. It is obtained by considering a periodic body-and-bar structure with two orbits of bodies represented by congruent regular cross-polytopes and $2d$ bars connecting a body in one orbit to as many bodies in the other orbit.

In dimension three, the cross-polytopes are regular octahedra with connections as shown in Figure 12. This type of periodic framework structure is found in crystalline materials related to Prussian blue, which have been studied for various properties dependent on framework flexibility [28, 34].

In higher dimensions, there are considerably more degrees of freedom for deformations than in the planar case and the proposed analogy will have inevitable limitations. For instance, there are nine degrees of freedom in dimension three [25] and regular cross-polytopes cannot produce a periodic tiling of R^d for $d \geq 3$. Nevertheless, when connecting bars are twice the edge length of the cross-polytopes, there are folding scenarios akin to the planar case.

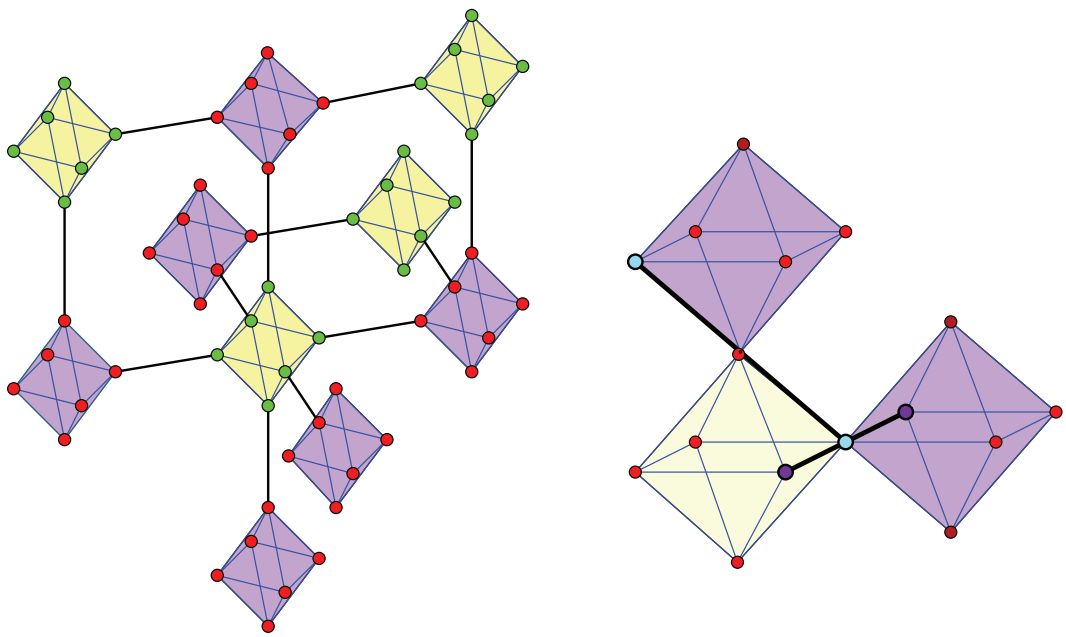

Figure 12. Left: fragment of a three-dimensional periodic framework akin to the deployed two-dimensional structure. Right: close-up for folding, with emphasis on two connecting bars and their endpoints.

We elaborate on the three-dimensional case and describe configurations via a yellow octahedron (centered at the origin) and the six purple octahedra connected to it. Folded configurations are imagined with connecting bars going along one edge of each pair, as shown on the right in Figure 12. This marks a Hamiltonian cycle on the 1-skeleton of the yellow octahedron. Periodicity can be satisfied by choosing the cycle to be centrally symmetric. Deployment can avoid self-intersection by keeping each connecting bar in the plane through the origin and its marked edge. The center of the attached purple octahedron remains in this plane, gradually stretching out toward alignment.

Remark. In dimension d, a centrally symmetric Hamiltonian cycle on the 1-skeleton of the cross-polytope with vertices at $\pm e_i$, $i = 1, \ldots, d$, is given by

$$e_1 \to e_2 \to \cdots \to e_d \to -e_1 \to -e_2 \to \cdots \to -e_d \to e_1.$$

8. Conclusion

We have considered a planar periodic framework with a rather well known structural pattern. The framework has remarkable deformation and deployment properties, which can be studied with complete geometrical rigor. Our investigation has emphasized the importance of the Gram map, which records the variation of the periodicity lattice on deformation. It may be observed that recourse to *algebraic geometry* is both natural and instrumental in this context.

Heuristically, the Gram map serves as a periodic version of the end-effector map in classical robotics. Thus, developments presented in Section 3 are a form of workspace determination and fundamentals for inverse kinematics.

Of particular relevance is the geometric treatment of *auxetic behavior*, which avoids reliance on the notion of Poisson's ratio. In the presence of several degrees of freedom, the distinction of auxetic from non-auxetic deformations is more subtle. The present case of three degrees of freedom is illuminated and resolved through Lorentzian geometry in dimension three.

The level of explicitness and precision attainable through our approach is enhanced by the presence of symmetry and the fact that all implicated framework configurations allow *ruler and compass* constructions.

Acknowledgements

The authors are grateful for the hospitality of the Radcliffe Institute for Advanced Study, Harvard University, in 2018–2019.

Funding

The authors disclosed receipt of the following financial support for the research, authorship, and/or publication of this article: This work was supported by the National Science Foundation (grant numbers 1704285 and 1703765) and the National Institutes of Health (grant number 1R01GM109456). **[AQ: 4]**

ORCID iD

Ciprian S. Borcea https://orcid.org/0000-0002-6207-9127

References

[1] Wojciechowski, KW. Two-dimensional isotropic system with a negative Poisson ratio. *Phys Lett A* 1989; 137(1,2): 60–64.
[2] Lakes, R. Deformation mechanisms in negative Poisson's ratio materials: Structural aspects. *J Mater Sci* 1991; 26: 2287.
[3] Prall, D and Lakes, RS. Properties of a chiral honeycomb with a Poisson's ratio of −1. *Int J Mech Sci* 1997; 39: 305–314.
[4] Sigmund, O, Torquato, S, and Askay, IA. On the design of 1-3 piezocomposites using topology optimization. *J Mater Res* 1998; 13: 1038–1048.
[5] Gaspar, N, Ren, XJ, Smith, CW, et al. Novel honeycombs with auxetic behaviour. *Acta Mater* 2005; 53: 2439–2445.
[6] Alderson, A, Alderson, KL, Attard, D, et al. Elastic constants of 3-, 4- and 6-connected chiral and anti-chiral honeycombs subject to uniaxial in-plane loading. *Compos Sci Technol* 2010; 70: 1042–1048.
[7] Rossiter, J, Takashima, K, Scarpa, F, et al. Shape memory polymer hexachiral auxetic structures with tunable stiffness. *Smart Mater Struct* 2014; 23: 045007.
[8] Frederickson, GN. *Hinged dissections: Swinging & twisting*. Cambridge: Cambridge University Press, 2002.
[9] Mitschke, H, Schwerdtfeger, J, Schury, F, et al. Finding auxetic frameworks in periodic tessellations. *Adv Mater* 2011; 23: 2669–2674.
[10] Mitschke, H, Robins, V, Mecke, K, et al. Finite auxetic deformations of plane tessellations. *Proc R Soc London, Ser A* 2013; 469: 20120465.
[11] Mitschke, H, Schury, F, Mecke, K, et al. Geometry: The leading parameter for the Poisson's ratio of bending-dominated cellular solids. *Int J Solids Struct* 2016; 100–101: 1–10.
[12] Mousanezhad, D, Haghpanah, B, Ghosh, R, et al. Elastic properties of chiral, anti-chiral, and hierarchical honeycombs: A simple energy-based approach. *Theor Appl Mech Lett* 2016; 6: 81–96.
[13] Jiang, Y, and Li, Y. 3D printed chiral cellular solids with amplified auxetic effects due to elevated internal rotation. *Adv Eng Mater* 2017; 19: 1600609.
[14] Idezak, E, and Strek, T. Minimization of Poisson's ratio in anti-tetra-chiral two-phase structure. *IOP Conf Ser: Mater Sci Eng* 2017; 248: 012006.
[15] Lim, TC. Analogies across auxetic models based on deformation mechanism. *Phys Status Solidi RRL* 2017; 11(6): 1600440.
[16] Bacigalupo, A, Gnecco, G, Lepidi, M, et al. Optimal design of low-frequency band gaps in anti-tetrachiral lattice meta-materials. *Composites, Part B* 2017; 115: 341–359.
[17] Barchiesi, E, Spagnuolo, M, and Placidi, L. Mechanical metamaterials: A state of the art. *Math Mech Solids* 2019; 24(1): 212–234.
[18] Wu, W, Qi, D, Liao, H, et al. Deformation mechanism of innovative 3D chiral metamaterials. *Sci Rep* 2018; 8: 12575.
[19] Wu, W, Hu, W, Qian, G, et al. Mechanical design and multifunctional applications of chiral mechanical metamaterials: A review. *Mater Des* 2019; 180: 107950.
[20] Farrugia, PS, Gatt, R, Lonardelli, EZ, et al. Different deformation mechanisms leading to auxetic behavior exhibited by missing rib square grid structures. *Phys Status Solidi B* 2019; 256: 1800186.
[21] Borcea, CS, and Streinu, I. Periodic frameworks and flexibility. *Proc R Soc London, Ser A* 2010; 466: 2633–2649.
[22] Borcea, CS, and Streinu, I. Liftings and stresses for planar periodic frameworks. *Discrete Comput Geom* 2015; 53: 747–782.
[23] Borcea, CS, and Streinu, I. Geometric auxetics. *Proc R Soc London, Ser A* 2015; 471: 20150033.
[24] Borcea, CS, and Streinu, I. Periodic auxetics: Structure and design. *Q J Mech Appl Math* 2018; 71(2): 125–138.
[25] Borcea, CS, Streinu, I, and Tanigawa, S. Periodic body-and-bar frameworks. *SIAM J Discrete Math* 2015; 29(1): 93–112.
[26] Müller, O, and Sánchez, M. An invitation to Lorentzian geometry. *Jahresber Dtsch Math-Ver* 2014; 115: 153–183.
[27] Borcea, CS, and Streinu, I. Kinematics of expansive planar periodic mechanisms. In: Lenarčič, J and Khatib, O (eds.) *Advances in robot kinematics*. Cham: Springer, 2014, 395–407.
[28] Goodwin, AL. Rigid unit modes and intrinsic flexibility of linearly bridged framework structures. *Phys Rev B* 2006; 74: 132302–132312.
[29] Lakes, R. Foam structures with a negative Poisson's ratio. *Science* 1987: 235; 1038–1040.

[30] Greaves, GN, Greer, AL, Lakes, R, et al. Poisson's ratio and modern materials. *Nat Mater* 2011; 10: 823–837.
[31] Lakes, RS. Negative-Poisson's-ratio materials: Auxetic solids. *Annu Rev Mater Res* 2017; 47: 63–81.
[32] Bertoldi, K, Vitelli, V, Christensen, J, et al. Flexible mechanical metamaterials. *Nat Rev Mater* 2017; 2: 17066.
[33] Sunada, T. *Topological crystallography*. Berlin: Springer, 2013.
[34] Goodwin, AL, Keen, DA, Tucker, MG, et al. Argentophilicity-dependent colossal thermal expansion in extended Prussian blue analogues. *J Am Chem Soc* 2008; 130: 9660–9661.